Rev.Adv.Mater.Sci. 12 (2006) 13-22

INCOMMENSURATE SPIN DYNAMICS IN UNDERDOPED CUPRATE PEROVSKITES

A. Sherman

Institute of Physics, University of Tartu, Riia 142, 51014 Tartu, Estonia

Received: November 12, 2005

Abstract. The incommensurate magnetic response observed in normal-state cuprate perovskites is interpreted based on Mori's projection operator formalism and the *t-J* model of Cu-O planes. In agreement with experiment, the calculated dispersion of maxima in the susceptibility has the shape of two parabolas with upward- and downward-directed branches which converge at the antiferromagnetic wave vector. The upper parabola reflects the dispersion of magnetic excitations of the localized Cu spins, while the lower parabola arises due to the weakness of the interaction between the spin excitations and holes near the hot spots. Also, in conformity with experiment, the low-frequency incommensurability parameter δ grows with the hole concentration x for $x \leq 0.12$ and then saturates. It is conjectured that the dissimilarity of the susceptibility frequency dependencies in yttrium and lanthanum cuprates may be connected with different values of the hole bandwidth and damping in these crystals.

1. INTRODUCTION

One of the most interesting features of the inelastic neutron scattering in lanthanum cuprates is that for hole concentrations $x \geq 0.04$, low temperatures, and small energy transfers, the scattering is peaked at incommensurate momenta $(1/2,1/2\pm\delta)$, $(1/2\pm\delta, 1/2)$ in the reciprocal lattice units $2\pi/a$ with the lattice period a [1]. For $x \leq 0.12$ the incommensurability parameter δ is approximately equal to x and saturates for larger concentrations [2]. The incommensurability was observed both below and above T_c [3]. The analogous low-frequency incommensurability was observed also in $YBa_2Cu_3O_{7-y}$ [4]. This gives ground to suppose that the incommensurability is a common feature of cuprate perovskites. However, the susceptibility for larger frequencies differs essentially in these two types of cuprates. A pronounced maximum is observed both below and above T_c at frequencies $\omega \approx 25$-40 meV in the underdoped $YBa_2Cu_3O_{7-y}$ and some other cuprates [5]. The magnetic response in the momentum space is sharply peaked at the antiferromagnetic wave vector $\boldsymbol{Q}=(1/2,1/2)$ for this frequency. Contrastingly, no maximum at such frequencies was observed in lanthanum cuprates. Instead, a broad feature was detected [6] for low temperatures and frequencies of several millielectronvolts. For even larger frequencies, the magnetic response becomes again incommensurate in both types of cuprates with maxima located at momenta $(1/2\pm\delta,1/2\pm\delta)$, $(1/2\pm\delta, 1/2\mp\delta)$ in some experiments [5,7-9]. In contrast to the low-frequency incommensurability in which the incom-

Corresponding author: A. Sherman, e-mail: alexei@fi.tartu.ee

mensurability parameter decreases with increasing frequency, the parameter of the high-frequency incommensurability grows with frequency. Thus, the dispersion of the maxima in the susceptibility resembles two parabolas with upward- and downward-directed branches which converge at the momentum $\boldsymbol{Q}$ and near the frequency ω_r [4,9].

The nature of the magnetic incommensurability is the subject of active discussion now. The most frequently used approaches for its explanation are based on the picture of itinerant electrons with the susceptibility calculated in the random phase approximation [10,11] and on the stripe picture [9,12]. In the former approach, the low-frequency incommensurability is connected with the Fermi surface nesting in the normal state or with the nesting in constant-energy contours in the superconducting state. This imposes rather stringent requirements on the hole spectrum, since the nesting has to persist in the range of hole concentrations $0.04 \le x \le 0.18$ where the incommensurability is observed and the nesting momentum has to change in a specific manner with doping to ensure the dependence $\delta(x)$ mentioned above. It is unlikely that these conditions are fulfilled in $La_{2-x}Sr_xCuO_4$ [13]. Besides, the applicability of the picture of itinerant electrons for underdoped cuprates casts doubts in view of a well-known feature of cuprates – strong electron correlations. As for the second notion, it should be noted that the charge-density wave connected with stripes in the elastic neutron scattering is observed only in crystals with the low-temperature tetragonal or the less-orthorhombic phases ($La_{2-y-x}Nd_ySr_xCuO_4$ and $La_{2-x}Ba_xCuO_4$) and is not observed in the $La_{2-x}Sr_xCuO_4$ crystal in the low-temperature orthorhombic phase [14]. At the same time, the magnetic incommensurability is similar in these phases. It can be supposed that the magnetic incommensurability is the cause rather than the effect of stripes which are formed when in-plane oxygen distortions favor the domain formation.

In the present work, the general formula for the magnetic susceptibility derived in Mori's projection operator formalism [15] is used for interpreting the experimental observations mentioned above. The *t-J* model of Cu-O planes is employed to describe spin excitations in the doped antiferromagnet. The hole spectrum is described by the data obtained either in the self-consistent calculations [16,17] or derived from the photoemission experiments [18,19]. In this approach the mentioned peculiarities of the magnetic properties of cuprates in the normal state are reproduced including the proper frequency and momentum location of the susceptibility maxima.

2. MAIN FORMULAS

To take proper account of strong electron correlations inherent in underdoped cuprates, we use the *t-J* model for the description of Cu-O planes and Mori's projection operator formalism for calculating Green's functions of Hubbard operators. Similar approaches were used for the Heisenberg and *t-J* models in Ref. [20]. The *t-J* model was shown to describe correctly the low-energy part of the realistic extended Hubbard model [21,22]. The Hamiltonian of the two-dimensional *t-J* model reads [23]

$$h = \sum_{\mathbf{nm}\sigma} t_{\mathbf{nm}} a^{+}_{\mathbf{n}\sigma} a_{\mathbf{m}\sigma} + \frac{1}{2}\sum_{\mathbf{nm}} J_{\mathbf{nm}} \mathbf{s}_{\mathbf{n}} \mathbf{s}_{\mathbf{m}}, \qquad (1)$$

where $a_{\mathbf{n}\sigma} = |\mathbf{n}\sigma\rangle\langle\mathbf{n}0|$ is the hole annihilation operator, $\boldsymbol{n}$ and $\boldsymbol{m}$ label sites of the square lattice formed by Cu ions, $\sigma=\pm1$ is the spin projection, $J_{\mathbf{nm}}$ and $t_{\mathbf{nm}}$ are the exchange and hopping constants, respectively, $|\mathbf{n}\sigma\rangle$ and $|\mathbf{n}0\rangle$ are states corresponding to the absence and presence of a hole on the site. These states can be considered as linear combinations of the products of the copper $3d_{x^2-y^2}$ and $2p_\sigma$ oxygen orbitals of the extended Hubbard model [22]. The spin–1/2 operators can be written as $s^z_n = 1/2\sum_\sigma \sigma|\mathbf{n}\sigma\rangle\langle\mathbf{n}\sigma|$ and $s^\sigma_{\mathbf{n}} = |\mathbf{n}\sigma\rangle\langle\mathbf{n},-\sigma|$.

Properties of the model are determined from the retarded hole and spin Green's functions

$$\begin{aligned} G(\mathbf{k}t) &= -i\theta(t)\langle\{a_{\mathbf{k}\sigma}(t), a^{+}_{\mathbf{k}\sigma}\}\rangle, \\ D(\mathbf{k}t) &= -i\theta(t)\langle[s^z_{\mathbf{k}}(t), s^z_{-\mathbf{k}}]\rangle, \end{aligned} \qquad (2)$$

where $a_{\boldsymbol{k}\sigma}$ and $s^z_{\mathbf{k}}$ are the Fourier transforms of the respective site operators, time dependencies of operators and the statistical averaging are defined with the Hamiltonian $H = h - \mu\sum_{\mathbf{n}} a^{+}_{\mathbf{n}\sigma} a_{\mathbf{n}\sigma}$ with the chemical potential μ. In Mori's projection operator formalism [15], the Fourier transforms of Green's functions (2) are calculated from the recursive relations

$$\begin{aligned} &R_n(\omega) = [\omega - E_n - R_{n+1}(\omega)F_n]^{-1}, \\ &n = 0,1,2,3\ldots \end{aligned} \qquad (3)$$

where $R_n(\omega)$ is the Laplace transform of $R_n(t) = |A_{nt}\cdot A^{+}_n||A_n\cdot A^{+}_n|^{-1}$, the definition of the inner product $|A\cdot B|$ depends on the type of Green's functions and for functions (2) it is $\langle\{A,B\}\rangle$ and $\langle[A,B]\rangle$ respectively, the time dependence in A_{nt} is determined by the relation

$$i\frac{d}{dt}A_{nt} = \prod_{k=0}^{n-1}(1-P_k)[A_{nt},H],\ A_{n,t=0} = A_n$$

with the projection operators P_k defined as $P_k B = \left|B\cdot A_k^+\right|\left|A_k\cdot A_k^+\right|^{-1}A_k$. The parameters E_n and F_n in relation (3) and the operators A_n in the functions R_n are calculated recursively in the procedure [24,25]

$$\begin{aligned}&[A_n,H] = E_nA_n + A_{n+1} + F_{n-1}A_{n-1},\\ &E_n = \left|[A_n,H]\cdot A_n^+\right|\left|A_n\cdot A_n^+\right|^{-1},\\ &F_{n-1} = \left|A_n\cdot A_n^+\right|\left|A_{n-1}\cdot A_{n-1}^+\right|^{-1},\ F_{-1}=0.\end{aligned} \tag{4}$$

We set $A_0=a_{\mathbf{k}\sigma}$ and $A_0 = s_{\mathbf{k}}^z$ for the functions (2) as the starting operators in procedures (3) and (4), respectively. Thus, $G(\mathbf{k}\omega) = R_0(\omega)\left\langle\left\{a_{\mathbf{k}\sigma},a_{\mathbf{k}\sigma}^+\right\}\right\rangle$ and $D(\mathbf{k}\omega) = R_0(\omega)\left\langle\left[s_{\mathbf{k}}^z,s_{-\mathbf{k}}^z\right]\right\rangle$. According Eq. (3), Green's functions are represented by continued fractions. Notice, however, that in the latter function $\left\langle\left[s_{\mathbf{k}}^z,s_{-\mathbf{k}}^z\right]\right\rangle = 0$ and therefore the above procedure cannot be directly used for the calculation of the spin Green's function. Instead we apply this procedure for calculating Kubo's relaxation function

$$\left(\left(s_{\mathbf{k}}^z,s_{-\mathbf{k}}^z\right)\right)_t = \theta(t)\int_t^\infty dt'\left\langle\left[s_{\mathbf{k}}^z(t'),s_{-\mathbf{k}}^z\right]\right\rangle$$

and use the relation

$$D(\mathbf{k}\omega) = \omega\left(\left(s_{\mathbf{k}}^z,s_{-\mathbf{k}}^z\right)\right)_\omega - \left(s_{\mathbf{k}}^z,s_{-\mathbf{k}}^z\right)$$

to derive Green's function. Here $\left(\left(s_{\mathbf{k}}^z,s_{-\mathbf{k}}^z\right)\right)_\omega$ is the Fourier transform of $\left(\left(s_{\mathbf{k}}^z,s_{-\mathbf{k}}^z\right)\right)_t$ and $(A,B) = i\int_0^\infty dt\langle[A(t),B]\rangle$ defines the inner product in the above recursive procedure for the case of Kubo's relaxation function.

To demonstrate the application of the above scheme, we calculate the spin Green's function. With Hamiltonian (1) and $A_0 = s_{\mathbf{k}}^z$ we find from Eq. (4)

$$\begin{aligned}&E_0\left(s_{\mathbf{k}}^z,s_{-\mathbf{k}}^z\right) = \left(i\dot{s}_{\mathbf{k}}^z,s_{-\mathbf{k}}^z\right) = \left\langle\left[s_{\mathbf{k}}^z,s_{-\mathbf{k}}^z\right]\right\rangle = 0,\\ &A_1 = A_1^s + A_1^h = \frac{1}{2\sqrt{N}}\times\\ &\sum_l e^{-i\mathbf{kl}}\left[\sum_{\mathbf{nm}}J_{\mathbf{nm}}(\delta_{\mathbf{ln}}-\delta_{\mathbf{lm}})s_{\mathbf{n}}^{+1}s_{\mathbf{m}}^{-1}\right.\\ &\left.+\sum_{\mathbf{nm}\sigma}\sigma t_{\mathbf{nm}}(\delta_{\mathbf{lm}}-\delta_{\mathbf{ln}})a_{\mathbf{n}\sigma}^+a_{\mathbf{m}\sigma}\right],\end{aligned} \tag{5}$$

where $i\dot{s} = \left[s_{\mathbf{k}}^z,H\right] = A_1$. To obtain a tractable form for the spin-excitation damping, it is convenient to approximate the quantity $\left(A_{1t},A_1^+\right)$ in $R_1(\omega)$ by the sum $\left(A_{1t}^s,A_1^{s+}\right) + \left(A_1^h(t),A_1^{h+}\right)$ where the second term describes the influence of holes on the spin excitations. Continuing calculations (4) with the first term of this sum, we get

$$F_0 = 4JC_1(\gamma_{\mathbf{k}}-1)\left(s_{\mathbf{k}}^z,s_{-\mathbf{k}}^z\right)^{-1},\ E_1 = 0, \tag{6}$$

where only the nearest neighbor interaction between spins was taken into account, $J_{\mathbf{nm}} = J\sum_a\delta_{\mathbf{n},\mathbf{m}+\mathbf{a}}$, the four vectors **a** connect neighbor sites, $\gamma_{\mathbf{k}} = 1/2\left[\cos(k_x)+\cos(k_y)\right]$ and $C_1 = \left\langle s_{\mathbf{n}}^{+1}s_{\mathbf{n}+\mathbf{a}}^{-1}\right\rangle$ is the spin correlation on neighbor sites. This parameter is connected with Green's function $D(\mathbf{k}\omega)$ by the relation

$$C_1 = -\frac{1}{\pi N}\sum_{\mathbf{k}}e^{i\mathbf{ka}}\int_{-\infty}^{\infty}d\omega[1+n_B(\omega)]\Im D(\mathbf{k}\omega),$$

$n_B = \left(e^{\omega/T}-1\right)^{-1}$, T is the temperature. Here we take into account that transversal and longitudinal spin correlations and Green's functions coincide up to the factor 2 due to the symmetry of Hamiltonian (1).

To calculate the quantity $\left(s_{\mathbf{k}}^z,s_{-\mathbf{k}}^z\right)$, let us notice that the interruption of the recursive calculations at this stage according to procedure (4) actually means that $\left(A_2,A_2^+\right)$ in the parameter F_1 is set to zero. $A_2 = i^2\ddot{s}_{\mathbf{k}}^z - F_0s_{\mathbf{k}}^z$ here. The substitution of this expression into $\left(A_2,A_2^+\right) = 0$ gives an equation for $\left(s_{\mathbf{k}}^z,s_{-\mathbf{k}}^z\right)$. Using the decoupling in $i^2\ddot{s}_{\mathbf{k}}^z$ we get [16]

$$\left(s_{\mathbf{k}}^z,s_{-\mathbf{k}}^z\right)^{-1} = 4\alpha J(\Delta+1+\gamma_{\mathbf{k}}), \tag{7}$$

where $\alpha\approx1$ is the decoupling parameter [26]. The meaning of the parameter Δ, which can be expressed in terms of spin correlations, will be discussed later.

Using the decoupling in $\left(A_1^h(t),A_1^{h+}\right)$, we find from the above formulas [25]

$$\Im D(\mathbf{k}\omega) = \frac{\omega\Im R(\mathbf{k}\omega)}{\left[\omega^2-\omega f_{\mathbf{k}}\Re R(\mathrm{k}\,\omega)-\omega_{\mathbf{k}}^2\right]^2+\left[\omega f_{\mathbf{k}}\Im R(\mathrm{k}\,\omega)\right]^2}, \tag{8}$$

where

$$\begin{aligned}&\omega_{\mathbf{k}}^2 = 16J^2\alpha|C_1|(1-\gamma_{\mathbf{k}})(\Delta+1+\gamma_{\mathrm{k}}),\\ &f_{\mathbf{k}}^{-1} = 4J|C_1|(1-\gamma_{\mathbf{k}}),\\ &\Im R(\mathbf{k}\omega) = \frac{8\pi\omega_{\mathbf{k}}^2}{N}\sum_{\mathbf{k}'}g_{\mathbf{kk}'}^2\int_{-\infty}^{\infty}d\omega'\\ &\times\frac{n_F(\omega+\omega')-n_F(\omega')}{\omega}A(\mathbf{k}'\omega')A(\mathbf{k}+\mathbf{k}',\omega+\omega'),\end{aligned} \tag{9}$$

the interaction constant $g_{\mathbf{kk'}} = t_{\mathbf{k'}} - t_{\mathbf{k+k'}}$ with $t_{\mathbf{k}} = \sum_{\mathbf{n}} e^{i\mathbf{k}(\mathbf{n}-\mathbf{m})} t_{\mathbf{nm}}$, $n_F(\omega) = \left(e^{\omega/T}+1\right)^{-1}$, $A(\mathbf{k}\omega) = -\pi^{-1}\Im G(\mathbf{k}\omega)$ is the hole spectral function. The real parts of $D(\mathbf{k}\omega)$ and $R(\mathbf{k}\omega)$ can be calculated from their imaginary parts and Kramers-Kronig relations.

If the hole hopping to nearest and next nearest sites is taken into account, the interaction constant $g_{\mathbf{kk'}}$ between holes and spin excitations acquires the form

$$g_{\mathbf{kk'}} = t\left(\gamma_{\mathbf{k'}} - \gamma_{\mathbf{k+k'}}\right) + t'\left(\gamma'_{\mathbf{k'}} - \gamma'_{\mathbf{k+k'}}\right), \qquad (10)$$

where $\gamma'_{\mathbf{k}} = \cos(k_x)\cos(k_y)$. The constant vanishes for $\mathbf{k}=\mathbf{Q}$ when the vector $\mathbf{k'}$ is located at the boundary of the magnetic Brillouin zone. In other words, fermions near hot spots interact weakly with spin excitations. As seen from Eq. (5), the operator $A_1 = is^z_{\mathbf{k}}$ which describes the time evolution of a spin excitation and an admixture of (or a decay to) fermion pairs, for $\mathbf{k}=\mathbf{Q}$ does not contain fermions at hot spots. This is connected with the short-range character of the interaction – the decaying spin excitation on site $\mathbf{n}$ creates the fermion pair on the same and neighboring sites [see Eq. (5)] which is reflected in the above form of the interaction constant.

An analogous procedure can be carried out for the hole Green's function and the obtained equations can be used for the self-consistent calculations of the hole and spin-excitation spectra. Such calculations were carried out in Refs. [16,17]. Along with these results, we used the hole dispersion derived from photoemission data [18,19]. To be specific, the calculations were carried out with the spectral function $A(\mathbf{k}\omega) \propto \left[\left(\omega - \varepsilon_{\mathbf{k}} + \mu\right)^2 + \eta^2\right]^{-1}$ with the hole dispersion

$$\begin{aligned}\varepsilon_{\mathbf{k}} &= -87.9 + 554.7\gamma_{\mathbf{k}} - 132.7\gamma'_{\mathbf{k}} - 13.2\gamma_{2\mathbf{k}} \\ &+92.45\left[\cos(2k_x)\cos(k_y) + \cos(k_x)\cos(2k_y)\right] \\ &-26.5\gamma'_{2\mathbf{k}}\end{aligned} \qquad (11)$$

proposed from the analysis of photoemission data in $Bi_2Sr_2CaCu_2O_8$ [18]. Here the coefficients are in millielectronvolts.

Notice that for low temperatures and a small hole damping the states with energies

$$-\omega < \varepsilon_{\mathbf{k'}} - \mu < 0 \text{ and } 0 < \varepsilon_{\mathbf{k+k'}} - \mu < \omega \qquad (12)$$

make the main contribution to the spin-excitation damping [see Eq. (9)].

The parameters t=0.5 eV, J=0.1 eV corresponding to hole-doped cuprates [27] were used in the self-consistent calculation. For the hole spectrum derived from photoemission, these parameters were utilized in Eqs. (8) and (9) for spin excitations together with parameters C_1, Δ, and α from self-consistent calculations [16,17]. The parameter t' was taken from the range [-0.4t,0].

3. THE SPIN-EXCITATION SPECTRUM

In Eq. (8), the quantity $\omega f_{\mathbf{k}} \Re R(\mathbf{k}\omega)$ influences the frequency of spin excitations only near the antiferromagnetic momentum $\mathbf{Q}$. Therefore it is convenient to incorporate this quantity in $\omega_{\mathbf{k}}$ which becomes the frequency of spin excitations. This modifies the parameter Δ. The most exact way to determine this parameter is to use the constraint of zero site magnetization

$$\left\langle s^z_{\mathbf{n}} \right\rangle = \frac{1}{2}(1-x) - \left\langle s^{-1}_{\mathbf{n}} s^{+1}_{\mathbf{n}} \right\rangle = 0. \qquad (13)$$

Notice that this constraint is fulfilled both in the short- and long-range antiferromagnetic ordering, in the latter case due to the statistical averaging over ordering directions. Using Eq. (8), it can be shown that $\Delta \propto \xi^{-2}$ where ξ is the correlation length of the short-range order. A positive value of Δ in this case leads to a finite frequency of spin excitations at $\mathbf{Q}$ which differentiates them from the classical antiferromagnetic magnons. The dispersion of spin excitations has a local minimum at $\mathbf{Q}$ and can be approximated as $\omega_{\mathbf{k}} = \left[\omega^2_{\mathbf{Q}} + c^2\left(\mathbf{k}-\mathbf{Q}\right)^2\right]^{1/2}$ near this momentum [see Eq. (9)]. In Fig. 1 the calculated dispersion of spin excitations near $\mathbf{Q}$ [25] is compared with the dispersion of maxima in the susceptibility in $YBa_2Cu_3O_{6.5}$ [5]. This is a bilayer crystal and the symmetry allows one to divide the susceptibility into odd and even parts. For the antiferromagnetic intrabilayer coupling the dispersion of the maxima in the odd part can be compared with our calculations carried out for a single layer. This comparison demonstrates that the observed dispersion of the susceptibility maxima above $\omega_{\mathbf{Q}}$ which we identify with the frequency ω_y is closely related to the dispersion of spin excitations.

4. MOMENTUM DEPENDENCE OF THE SUSCEPTIBILITY

The imaginary part of the magnetic susceptibility $\chi''(\mathbf{k}\omega)$ which determines the dynamic structure factor measured in neutron-scattering experiments [29] is connected with the spin Green's function by the relation

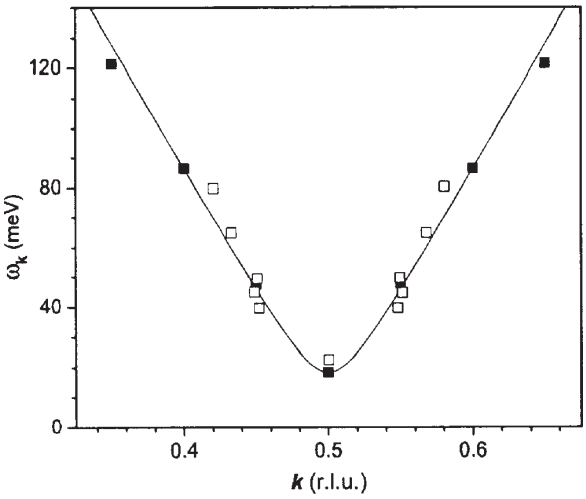

Fig. 1. The dispersion of spin excitations calculated self-consistently in a 20×20 lattice for x=0.06 and T=17K [25] (filled squares). The solid line is the fit of the dependence $\omega_{\mathbf{k}} = \left[\omega_{\mathbf{Q}}^2 + c^2(\mathbf{k}-\mathbf{Q})^2\right]^{1/2}$ to these data. Open squares are positions of maxima in the odd susceptibility in $YBa_2Cu_3O_{6.5}$ (x≈0.075 [28]) at T=5K [5].

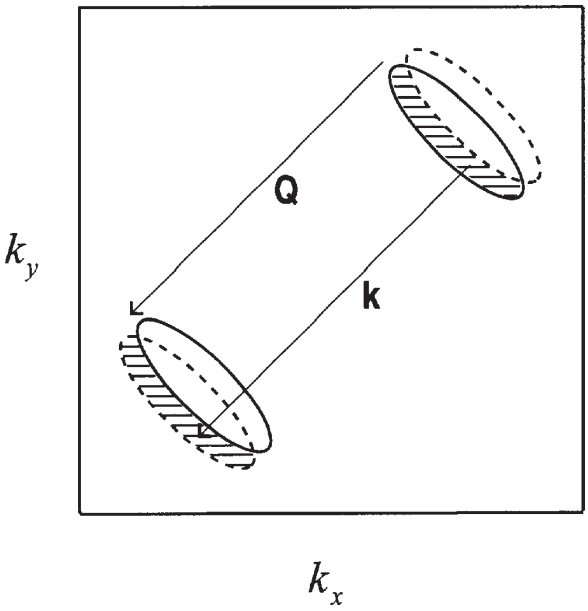

Fig. 2. The Brillouin zone of the square lattice. Solid curves are two of four ellipses forming the Fermi surface at small x. Dashed lines are the Fermi-surface contours shifted by ±(**k**-**Q**). Regions of **k**′ and **k** + **k**′ contributing to the damping (9) are shaded.

$$\chi''(\mathbf{k}\omega) = -4\mu_B^2 \Im D(\mathbf{k}\omega), \tag{14}$$

where μ_B is the Bohr magneton. First, we consider the case of small transfer frequencies when Eq. (8) reduces to

$$\Im D(\mathbf{k}\omega) = \omega\omega_{\mathbf{k}}^{-4} \Im R(\mathbf{k}\omega). \tag{15}$$

As seen from Eq. (9) and Fig. 1, $\omega^{-4}_{\mathbf{k}}$ is a decreasing function of the difference **k**-**Q** which acts in favor of a commensurate maximum peaked at **Q** in the momentum dependence of the susceptibility. However, if $\Im R(\mathbf{k}\omega)$ has a pronounced dip at the antiferromagnetic momentum, the commensurate maximum splits into several incommensurate peaks. Since for small ω hole states near the Fermi level make the main contribution to the spin-excitation damping [see Eq. (12)] and Fermi surfaces are different for light and moderate doping [16,17], these two cases have to be considered separately.

Two of four ellipses centered at $(\pm\pi/2, \pm\pi/2)$ which form the Fermi surface for small x are shown in Fig. 2. According to Eq. (9), a decaying spin excitation at low temperatures creates a fermion pair with a hole with the momentum **k**′ in one of the ellipses and an electron at **k**+**k**′. However, for **k**=**Q**, the state with the wave vector **Q**+**k**′ is below the Fermi level due to the nesting of the ellipses with the wave vector **Q**. Thus, the spin-excitation damping vanishes in these conditions. As **k** recedes from **Q,** the possibility arises to create the fermion pair in the shaded regions in Fig. 2. The area of these regions and the value of $\Im R(\mathbf{k}\omega)$ grow with the distance of **k** from **Q**. Hence $\Im R(\mathbf{k}\omega)$ does have a dip at the antiferromagnetic momentum [30].

The Fermi surface for the band (11) is shown in Fig. 3. This type of the Fermi surface corresponds to the case of moderate doping [16,17]. As follows from Eq. (12), for low temperatures, frequencies and **k**=**Q** hole states which make the main contribution to the spin-excitation damping (9) are located near the hot spots. However, as indicated above, the interaction constant $g_{\mathbf{Qk}'}$, Eq. (10), for these wave vectors is small; this fact leads to the smallness of $\Im R(\mathbf{Q}\omega)$. With the wave vector moving away from **Q**, momenta of states contributing to the spin-excitation damping recede from the hot spots, the interaction constant grows as well as the spin-excitation damping. Thus, the damping has a dip at **Q** in

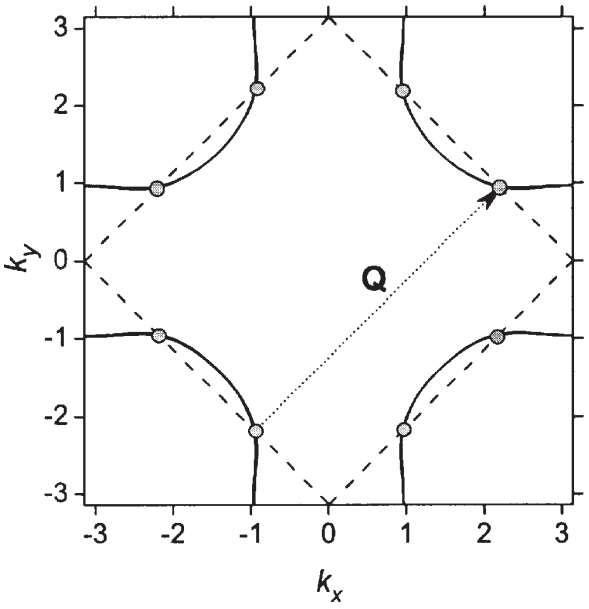

Fig. 3. The Fermi surface for dispersion (11) and μ=-40 meV (solid lines). Dashed lines show the boundary of the magnetic Brillouin zone, gray circles are the hot spots, the dotted arrow is the antiferromagnetic momentum **Q**.

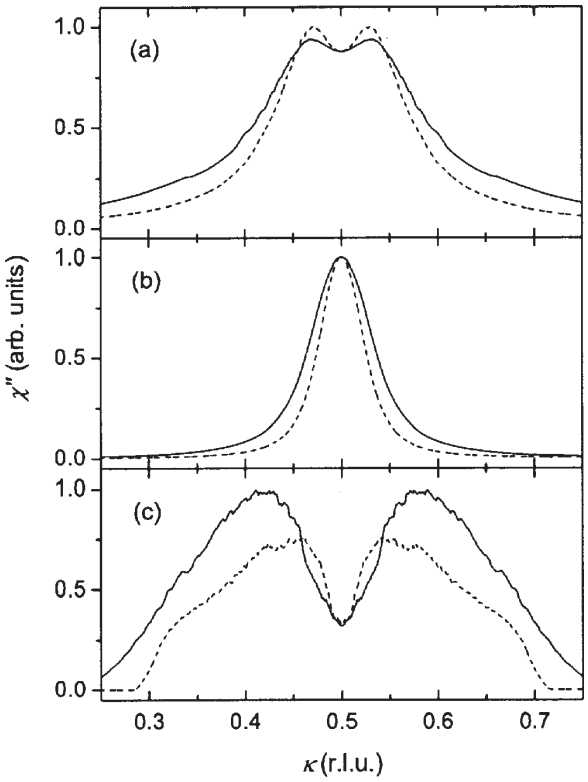

Fig. 4. The momentum dependence of $\chi''(\mathbf{k}\omega)$ for T=0, $x\approx$0.12, $\mu\approx$-40 meV, t'=-0.2t and ω=70 meV, η=30 meV (a), ω=35 meV, η=15 meV (b), ω=2 meV, η=1.5 meV (c). Calculations were carried out in a 1200×1200 lattice. The solid lines correspond to scans along the edge of the Brillouin zone, $\mathbf{k}=(\kappa,1/2)$ the dashed lines are for the zone diagonal, $\mathbf{k}=(\kappa,\kappa)$.

this case also; it leads to the low-frequency incommensurability [31].

The momentum dependence of the susceptibility corresponding to this latter case is shown in Fig. 4c. The calculations were carried out using the dispersion (11). Analogous results were also obtained with other dispersions found in literature [18,19]. As seen from the figure, the susceptibility for small frequencies is peaked at the wave vectors $\mathbf{k}=(1/2,1/2\pm\delta)$ and $(1/2\pm\delta,1/2)$. Similar momentum dependencies of $\chi''(\mathbf{k}\omega)$ were observed in yttrium and lanthanum cuprates [3,4,9].

The dependence of the incommensurability parameter δ on x calculated for ω=2 meV is shown in Fig. 5. The value of δ for x=0.043 was obtained with the low-concentration hole dispersion, other points – with dispersion (11). In agreement with experiment (see the inset) δ grows with x up to $x\leq$0.12 and then saturates. In our calculations, this dependence is solely conditioned by the behavior of the spin-gap frequency ω_Q which for small hole concentrations grows as $x^{1/2}$ and saturates near x=0.12 [16]. The growth of the spin-gap frequency leads to a weaker momentum dependence of the spin-excitation frequency ω_k near **Q** which increases the distance between susceptibility maxima in Eq. (15).

The above discussion concerned with transfer frequencies $\omega\leq\omega_Q$ If the frequency is close or larger then the gap frequency w_Q, the resonance denominator in Eq. (8) starts to determine the momentum dependence of the susceptibility. If the spin excitations are not overdamped, the equation $\omega=\omega_k$ for $\omega\geq\omega_Q$ defines the position of the maxima in $\chi''(\mathbf{k}\omega)$ which are somewhat shifted by the momentum dependence of the spin-excitation damping $f_k\Im R(\mathbf{k}\omega)$. Using the mentioned approximation $\omega_k=\left[\omega_Q^2+c^2(\mathbf{k}-\mathbf{Q})^2\right]^{1/2}$, we find that the maxima are located near a circle centered at **Q** with the radius $c^{-1}\left(\omega^2-\omega_Q^2\right)^{1/2}$ [32,25]. Thus, for $\omega\approx\omega_Q$, the

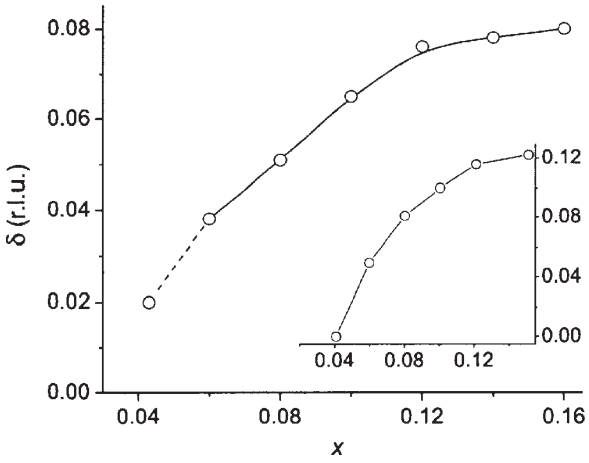

Fig. 5. The incommensurability parameter δ vs. x for ω=2 meV. Inset: experimental data [2] for $La_{2-x}Sr_xCuO_4$. Connecting lines are a guide to the eye.

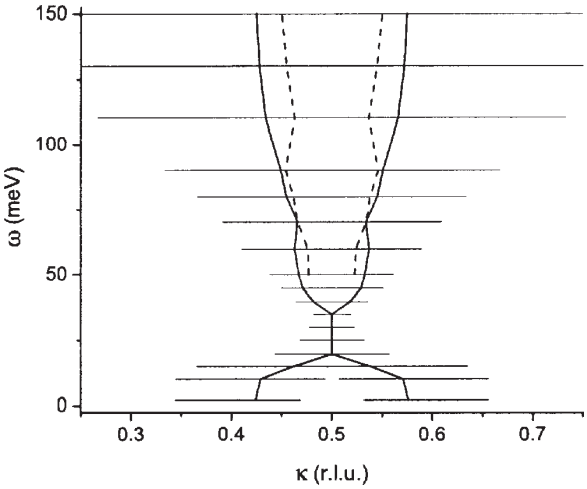

Fig. 6. The dispersion of maxima in $\chi''(\mathbf{k}\omega)$ for scans along the edge [$\mathbf{k} = (\kappa, 1/2)$, solid lines] and along the diagonal [$\mathbf{k} = (\kappa, \kappa)$, dashed lines] of the Brillouin zone. The dispersion along the diagonal is shown only in the frequency range in which these maxima are more intensive than those along the edge. Parameters are the same as in Fig. 4. Horizontal bars are FWHM for maxima along the edge of the Brillouin zone.

magnetic response is commensurate – $\chi''(\mathbf{k}\omega)$ is peaked at **Q**. For larger ω, the commensurate maximum splits into incommensurate peaks with distances from the antiferromagnetic momenta which grow with the frequency. Such situations are shown in Figs. 4a and 4b. $\omega_Q \approx 37$ meV for parameters of Fig. 4. With these parameters, incommensurate maxima for $\omega > \omega_Q$ are located at $\mathbf{k} = (1/2 \pm \delta, 1/2 \pm \delta)$, $(1/2 \pm \delta, 1/2 \mp \delta)$, in contrast to the low-frequency maxima at $(1/2, 1/2 \pm \delta)$, $(1/2 \pm \delta, 1/2)$. A similar location of the high-frequency maxima was observed in $YBa_2Cu_3O_{7-y}$ and $La_{2-x}Ba_xCuO_4$ [4,8,9]. However, for other parameters, e.g., for increased hole damping, maxima were found to form a circle or merge together in a broad commensurate maximum. Such situations were also observed experimentally [33]. For parameters of Fig. 4, the dispersion of maxima in $\chi''(\mathbf{k}\omega)$ for scans along the edge and the diagonal of the Brillouin zone and their full widths at half maximum (FWHM) are shown in Fig. 6. Analogous dispersions were observed in lanthanum and yttrium cuprates [4,9] and obtained in Ref. [18] in the itinerant-carrier approach for the superconducting state with the use of dispersion (11).

5. FREQUENCY DEPENDENCE OF THE SUSCEPTIBILITY

The frequency dependencies of the magnetic susceptibility at the antiferromagnetic momentum are shown in Fig. 7. Our results for the normal state were obtained from the data of the self-consistent calculations [16,25]. A small frequency-independent spin-excitation damping was added to the value described by Eq. (9) to obtain a better fit of the shape of the calculated susceptibility to the experimental data. This additional damping influences weakly the position of the maximum in the susceptibility. As seen from the figure, the *t-J* model is able to reproduce correctly the location of the maximum in the susceptibility and gives a proper evolution of this maximum with doping. The temperature variation of the maximum is also reproduced correctly [25]. For the parameters of Fig. 7, the location of the maximum coincides approximately with the value of the spin gap ω_Q and is determined by the resonance denominator in Eq. (8). Comparing the spin-excita-

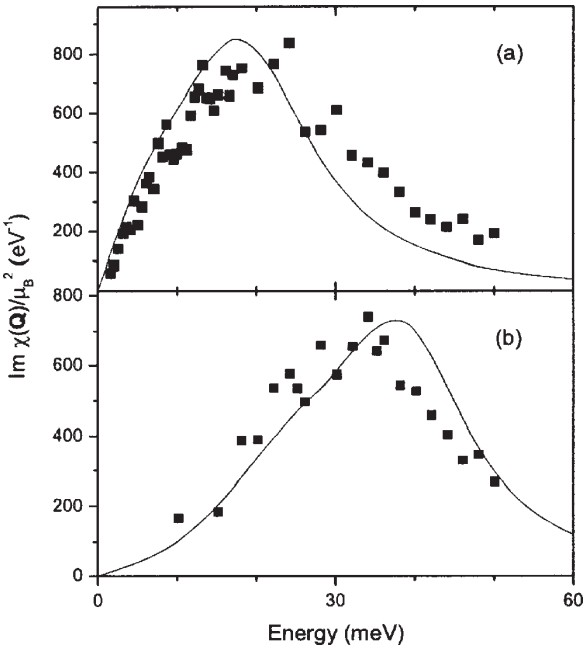

Fig. 7. The frequency dependence of $\chi''(\mathbf{Q}\omega)$. Curves are our results obtained with the hole spectrum from Ref. [16] for T=116K, x=0.06 (a), and x=0.12 (b). Filled squares are the odd susceptibility measured [5] in $YBa_2Cu_3O_{6.5}$ [(a), $x\approx0.075$] and $YBa_2Cu_3O_{6.83}$ [(b), $x\approx0.14$] at T=100K.

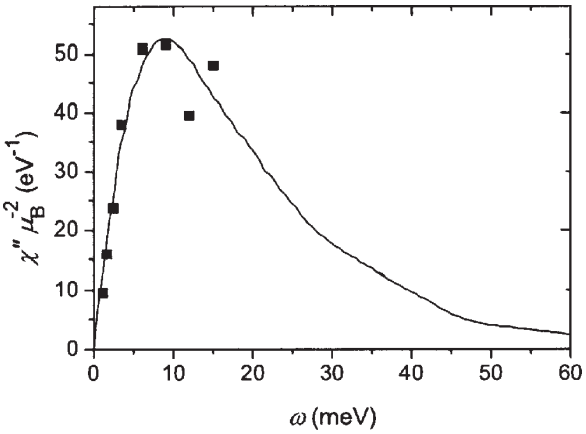

Fig. 8. The frequency dependence of $\chi''(\mathbf{Q}\omega)$. The solid curve was calculated for $x\approx0.12$, T=0, **k**=(0.42,0.5) and dispersion (11) scaled by the factor 0.4. Squares are the susceptibility in $La_{1.86}Sr_{0.14}CuO_4$ for T=35K at the incommensurate peak [6].

tion damping with the gap frequency, we found that the spin excitations are not overdamped near **Q**. In view of the similarity in shapes of the experimental and calculated curves, the same conclusion can be made with respect to the spin excitations in the underdoped $YBa_2Cu_3O_{7-y}$. Similar results were obtained with the hole dispersions (11).

The value of the spin-excitation damping was found to depend heavily on details of the hole band such as the bandwidth, damping, and the distribution of the spectral weight. Changes in these parameters may lead to overdamping of spin excitations. In this case, the position of the maximum in the frequency dependence of χ'' has nothing to do with the spin-excitation frequency. An example of such changes is shown in Fig. 8 where the susceptibility was calculated with dispersion (11) scaled by the factor 0.4. The calculations were carried out for **k**=(0.42,0.5) which corresponds to the momentum of the low-frequency peak in Fig. 4c. In this case, excitations near the spin gap are overdamped and it leads to the red shift of the susceptibility maximum. The similar frequency dependence of χ'' without a well-defined peak of spin excitations is observed in $La_{2-x}Sr_xCuO_4$ [6]. Thus, we suppose that the observed dissimilarity in the frequency dependencies of the susceptibility in lanthanum and yttrium cuprates may be connected with some difference in their hole spectra.

The increased spin-excitation damping obtained above with the scaling of the hole dispersion does not affect markedly the low-frequency incommensurability. However, we found broad commensurate maxima only for the frequencies $\omega_Q<\omega<150$ meV instead of the incommensurate peaks shown in Fig. 4a.

6. CONCLUDING REMARKS

Mori's projection operator formalism and the *t-J* model of Cu-O planes were used for the interpretation of the magnetic susceptibility in cuprate perovskites. It was shown that the calculated momentum and frequency dependencies of the imagi-

nary part of the susceptibility χ'', the dispersion and location of maxima in it, and the concentration dependence of the incommensurability parameter are similar to those observed in lanthanum and yttrium cuprates. The dispersion of the maxima in χ'' resembles two parabolas with upward- and downward-directed branches which converge at the antiferromagnetic wave vector **Q** and at the respective frequency of spin excitations $\omega_{\mathbf{Q}}$ This frequency corresponds to a local minimum in the dispersion of spin excitations and its value is connected with the correlation length of the short-range antiferromagnetic order. We relate the upper parabola to the spin-excitation dispersion. The incommensurability connected with the lower parabola is related to the dip in the spin-excitation damping at **Q**. For light doping, this dip is a consequence of the nesting of the ellipses forming the Fermi surface. For moderate doping, the dip arises due to the smallness of the interaction between spin excitations and holes near the hot spots, which is a consequence of the short-range character of this interaction. In agreement with experiment, the incommensurate peaks which form the lower parabola are located at momenta $(1/2, 1/2 \pm \delta)$ and $(1/2 \pm \delta, 1/2)$ while peaks in the upper parabola are at $(1/2 \pm \delta, 1/2 \pm \delta)$ and $(1/2 \pm \delta, 1/2 \mp \delta)$. The behaviour of the low-frequency incommensurability parameter δ is also in agreement with experiment; it grows linearly with the hole concentration x for $x \leq 0.12$ and then saturates. This behavior of δ is mainly connected with the concentration dependence of the frequency $\omega_{\mathbf{Q}}$ of the spin gap at the antiferromagnetic wave vector. We found that the incommensurability disappears for the transfer frequencies $\omega < \omega_{\mathbf{Q}}$ if the damping of holes with energies $\pm\omega$ is greater than ω. This incommensurability vanishes also when the chemical potential approaches the extended van Hove singularities at $(0,\pi)$ and $(\pi,0)$ The incommensurability for $\omega > \omega_{\mathbf{Q}}$ disappears for large spin-excitation damping. The value of this damping depends heavily on the hole damping and on the shape and width of the hole band. We suppose that the marked difference in the frequency dependencies of the susceptibility in $YBa_2Cu_3O_{7-y}$ and $La_{2-x}Sr_xCuO_4$ – a pronounced peak at $\omega \approx 25$-40 meV for $\mathbf{k}=\mathbf{Q}$ in the former crystal and a broad feature at $\omega < 10$ meV in the latter – is a consequence of the difference in the electron spectra. The larger spin-excitation damping in $La_{2-x}Sr_xCuO_4$ leads to overdamping of spin excitations, while in the underdoped $YBa_2Cu_3O_{7-y}$ the excitations are well-defined even in the normal state.

ACKNOWLEDGEMENTS

This work was partially supported by the ESF grant No. 5548 and by the DFG.

REFERENCES

[1] H. Yoshizawa, S. Mitsuda, H. Kitazawa and K. Katsumata // *J. Phys. Soc. Japan* **57** (1988) 3686; R.J. Birgeneau, Y. Endoh, Y. Hidaka, K. Kakurai, M.A. Kastner, T. Murakami, G. Shirane, T.R. Thurston and K. Yamada // *Phys. Rev. B* **39** (1989) 2868.

[2] K. Yamada, C.H. Lee, K. Kurahashi, J. Wada, S. Wakimoto, S. Ueki, H. Kimura, Y. Endoh, S. Hosoya, G. Shirane, R.J. Birgeneau, M. Greven, M.A. Kastner and Y.J. Kim // *Phys. Rev. B* **57** (1998) 6165.

[3] T.E. Mason, G. Aeppli, S.M. Hayden, A.P. Ramirez and H.A. Mook // *Phys. Rev. Lett.* **71** (1993) 919; M. Matsuda, K. Yamada, Y. Endoh, T.R. Thurston, G. Shirane, R.J. Birgeneau, M.A. Kastner, I. Tanaka and H. Kojima // *Phys. Rev. B* **49** (1994) 6958.

[4] P. Dai, H.A. Mook and F. Dogan // *Phys. Rev. Lett*. **80** (1998) 1738; M. Arai, T. Nishijima, Y. Endoh, T. Egami, S. Tajima, K. Tamimoto, Y. Shiohara, M. Takahashi, A. Garrett and S.M. Bennington // *Phys. Rev. Lett.* **83** (1999) 608; P. Bourges, Y. Sidis, H.F. Fong, L.P. Regnault, J. Bossy, A. Ivanov and B. Keimer // *Science* **288** (2000) 1234.

[5] P. Bourges, In: T*he Gap Symmetry and Fluctuations in High Temperature Superconductors*, ed. by J. Bok, G. Deutscher, D. Pavuna and S.A. Wolf (Plenum Press: New York, 1998), p. 349; H. He, Y. Sidis, P. Bourges, G.D. Gu, A. Ivanov, N. Koshizuka, B. Liang, C.T. Lin, L.P. Regnault, E. Schoenherr and B. Keimer // *Phys. Rev. Lett.* **86** (2001) 1610.

[6] G. Aeppli, T.E. Mason, S.M. Hayden, H.A. Mook and J. Kulda // *Science* **279** (1997) 1432.

[7] S.M. Hayden, G. Aeppli, H.A. Mook, T.G. Perring, T.E. Mason, S.-W. Cheong and Z. Fisk // *Phys. Rev. Lett*. **76** (1996) 1344.

[8] S.M. Hayden, H.A. Mook, P. Dai, T.G. Perring and F. Doğan // *Nature* **429** (2004) 531.

[9] J.M. Tranquada, H. Woo, T.G. Perring, H. Goka, G.D. Gu, G. Xu, M. Fujita and K. Yamada // *Nature* **429** (2004) 534.

[10] D.Z. Liu, Y. Zha and K. Levin // *Phys. Rev. Lett.* **75** (1995) 4130; N. Bulut and D.J. Scalapino // *Phys. Rev. B* **53** (1996) 5149.
[11] J. Brinckmann and P.A. Lee // *Phys. Rev. Lett.* **82** (1999) 2915.
[12] V. Hizhnyakov and E. Sigmund // *Physica C* **156** (1988) 655; J. Zaanen and O. Gunnarsson // *Phys. Rev. B* **40** (1989) R7391; K. Machida // *Physica C* **158** (1989) 192; G. Seibold and J. Lorenzana // *Physica B* **359-361** (2005) 548.
[13] A. Ino, C. Kim, M. Nakamura, T. Yoshida, T. Mizokawa, A. Fujimori, Z.X. Shen, T. Kakeshita, H. Eisaki and S. Uchida // *Phys. Rev. B* **65** (2002) 094504.
[14] H. Kimura, K. Hirota, H. Matsushita, K. Yamada, Y. Endoh, S.-H. Lee, C.F. Majkrzak, R. Erwin, G. Shirane, M. Greven, Y.S. Lee, M.A. Kastner and R.J. Birgeneau // *Phys. Rev. B* **59** (1999) 6517; M. Fujita, H. Goka, K. Yamada and M. Matsuda // *Phys. Rev. Lett*. **88** (2002) 167008.
[15] H. Mori // *Progr. Theor. Phys.* **34** (1965) 399.
[16] A. Sherman and M. Schreiber // *Eur. Phys. J. B* **32** (2003) 203.
[17] A. Sherman // *Phys. Rev. B* **70** (2004) 184512.
[18] M.R. Norman // *Phys. Rev. B* **61** (2000) 14751.
[19] R.J. Radtke and M.R. Norman // *Phys. Rev. B* **50** (1994) 9554; M.C. Schabel, C.-H. Park, A. Matsuura, Z.-X. Shen, D.A. Bonn, R. Liang and W.N. Hardy // *Phys. Rev. B* **57** (1998) 6090.
[20] Yu.A. Tserkovnikov // *Theor. Math. Phys*. **52** (1983) 712; G. Jackeli and N.M. Plakida // *Theor. Math. Phys.* **114** (1998) 335; S. Winterfeldt and D. Ihle // *Phys. Rev. B* **58** (1998) 9402; I.A. Larionov // *Phys. Rev. B* **69** (2004) 214525.
[21] F.C. Zhang and T.M. Rice // *Phys. Rev. B* **37** (1988) 3759.
[22] J.H. Jefferson, H. Eskes and L.F. Feiner // *Phys. Rev. B* **45** (1992) 7959; A.V. Sherman // *Phys. Rev. B* **47** (1993) 11521.
[23] E. Dagotto // Rev. Mod. Phys. **66** (1994) 763; Yu.A. Izyumov // *Usp. Fiz. Nauk* **167** (1997) 465, in Russian [*Phys.-Usp. (Russia)* **40** (1997) 445].
[24] A.V. Sherman // *J. Phys. A* **20** (1987) 569.
[25] A. Sherman and M. Schreiber // *Phys. Rev. B* **65** (2002) 134520; B **68** (2003) 094519.
[26] J. Kondo and K. Jamaji // *Progr. Theor. Phys.* **47** (1972) 807.
[27] A.K. McMahan, J.F. Annett and R.M. Martin // *Phys. Rev. B* **42** (1990) 6268; V.A. Gavrichkov, S.G. Ovchinnikov, A.A. Borisov and E.G. Goryachev // *Zh. Eksp. Teor. Fiz.* **118** (2000) 422, in Russian [JETP (Russia) **91** (2000) 369].
[28] J.L. Tallon, C. Bernhard, H. Shaked, R.L. Hitterman and J.D. Jorgensen // *Phys. Rev. B* **51** (1995) R12911.
[29] M.A. Kastner, R.J. Birgeneau, G. Shirane and Y. Endoh // *Rev. Mod. Phys.* **70** (1998) 897.
[30] A. Sherman and M. Schreiber // *Phys. Rev. B* **69** (2004) 100505(R).
[31] A. Sherman // *Phys. Lett. A* **337** (2005) 435; A. Sherman and M. Schreiber // *Int. J. Modern Phys. B* **19** (2005) 2145.
[32] V. Barzykin and D. Pines // *Phys. Rev. B* **52** (1995) 13585.
[33] Y. Endoh, T. Fukuda, S. Wakimoto, M. Arai, K. Yamada and S.M. Bennington // *J. Phys. Soc. Japan* **69**, *Suppl. B* (2000) 16; C. Stock, W.J.L. Buyers, R.A. Cowley, P.S. Clegg, R. Coldea, C.D. Frost, R. Liang, D. Peets, D. Bonn, W.N. Hardy and R.J. Birgeneau // *Phys. Rev. B* **71** (2005) 024522.